ACS APPLIED MATERIALS & INTERFACES
Research Article
www.acsami.org

Interface Properties of Atomic Layer Deposited TiO_2/Al_2O_3 Films on $In_{0.53}Ga_{0.47}As$/InP Substrates

C. Mukherjee,[†,‡] T. Das,*[,†] C. Mahata,[†] C. K. Maiti,[†] C. K. Chia,[§] S. Y. Chiam,[§] D. Z. Chi,[§] and G. K. Dalapati*[,§]

[†]VLSI Engineering Lab, Department of Electronics and ECE, Indian Institute of Technology-Kharagpur, India 721302

[§]Institute of Materials Research and Engineering, A*STAR (Agency for Science, Technology and Research), 3 Research Link, Singapore 117602

ABSTRACT: Electrical and interfacial properties of metal-oxide-semiconductor (MOS) capacitors fabricated using atomic layer deposited bilayer TiO_2/Al_2O_3 films on $In_{0.53}Ga_{0.47}As$/InP substrates are reported. Vacuum annealing at 350 °C is shown to improve the interface quality. Capacitance−voltage ($C-V$) characteristics with higher accumulation capacitance, negligible frequency dispersion, small hysteresis and low interface state density (~1.5×10^{11} cm^{-2} eV^{-1}) have been observed for MOS capacitors. Low frequency ($1/f$) noise characterization and inelastic electron tunneling spectroscopy (IETS) studies have been performed to determine defects and interface traps and explain the lattice dynamics and trap state generation mechanisms. Both the IETS and $1/f$ noise studies reveal the spatial locations of the traps near the interface and also the nature of the traps. The IETS study further revealed the dynamic evolution of trap states related to low frequency noise sources in the deposited TiO_2/Al_2O_3 stacks. It is shown that deposition of an ultrathin layer of TiO_2 on Al_2O_3 can effectively control the diffusion of As in the dielectric and the oxidation states of In and Ga at the $In_{0.53}Ga_{0.47}As$ surface.

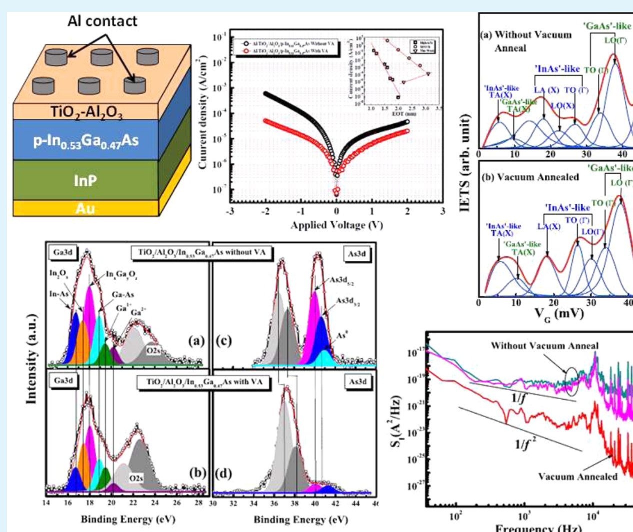

KEYWORDS: *atomic layer deposition, vacuum annealing, InGaAs, low-frequency noise, inelastic electron tunneling spectroscopy, lattice dynamics, traps*

1. INTRODUCTION

Recently, III−V compound semiconductors have received intense research interest as possible channel material in MOSFETs because of their high bulk electron mobility and breakdown field compared to that of silicon.[1] The ternary alloy, such as $In_{0.53}Ga_{0.47}As$ with lattice matched to InP, is one of the most attractive materials because of its high low-field electron mobility and high saturation velocity. Thermodynamic instability and poor quality of the gate insulator (low active defect density is essential to avoid Fermi level pinning at the interface) have so far impeded their use as channel materials.[2] It is thus important to find suitable gate dielectrics and develop optimum passivation techniques for III−V semiconductor surfaces. Alternative high-k gate dielectrics provide an opportunity for considering III−V compound semiconductors as channel materials in MOSFET applications.[3,4]

Atomic layer deposition (ALD) Al_2O_3 is known to provide a relatively low interface defect density during growth[5,6] and an unpinned Fermi level on InGaAs (100) substrates. Al_2O_3 has a moderate dielectric constant compared to other high-k oxides and is known to provide a relatively low interface defect density and an unpinned Fermi level on InGaAs(100) substrates. Low dielectric constant of Al_2O_3 hinders scaling of gate oxide capacitance density,[7] and also the hysteresis voltage is high.[8] On the other hand, titanium dioxide (TiO_2) has a wide range of dielectric constant of 10−86, and is a potential candidate as gate oxide in InGaAs MOSFETs. Surface passivation of III−V substrates using TiO_2 has shown that the hysteresis voltage is low compared to other dielectrics, but the presence of a thick interfacial layer is observed for directly deposited TiO_2.[9] Thus, it is difficult to find a single dielectric which satisfies all the requirements for end-of-roadmap MOS gate dielectrics (high dielectric constant, low interface trap density, high thermal stability, etc.), making bilayer gate dielectrics an interesting option. Over the past decade, various efforts to improve MOS capacitor performance have focused on understanding the device physics, optimizing the morphology through advanced process-

Received: November 12, 2013
Accepted: January 28, 2014
Published: January 28, 2014

ACS Publications © 2014 American Chemical Society

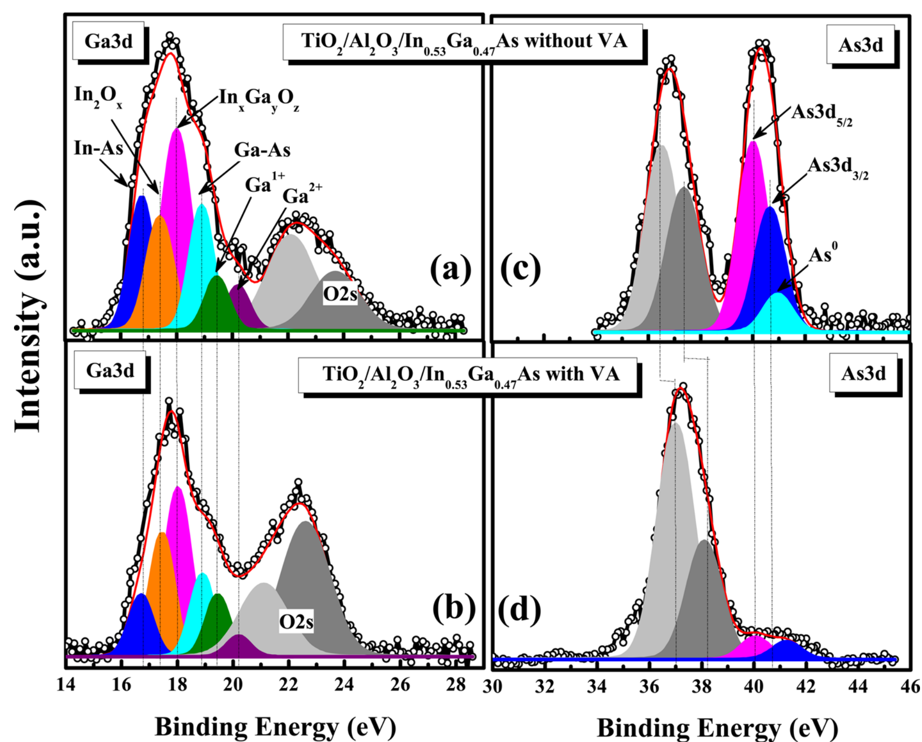

Figure 1. (a, b) Ga 3d and (c, d) As 3d core-level spectra from TiO_2/Al_2O_3 /$In_{0.53}Ga_{0.47}As$ gate stack with and without vacuum annealing.

ing methods, and developing high performance dielectric materials.

The performance of MOS devices is critically dependent on the properties of both the active materials and their interfaces. When the gate dielectric is only a few atomic layers thick, conventional dielectric characterization tools, such as infrared spectroscopy and Raman spectroscopy are ineffective in revealing structural and compositional information of the gate oxide. In contrast, the inelastic electron tunneling spectroscopy (IETS) technique is more sensitive for metal-oxide-semiconductor structures with ultrathin gate dielectrics,[10] and is suitable in the study of phonon density of states, superconducting gaps, electrode phonons, barrier phonons and electron density of states[11,12] of high-k dielectrics.[13] A wide variety of information about MOS capacitors can be obtained by IETS with excellent sensitivity and resolution, including: phonon modes of the gate electrodes, dielectric, and substrate; various vibrational modes of the bonding structures at interfaces; impurities in the gate dielectric and at interfaces; trap features and other electronic defects. It has long been known that the low frequency noise behavior of MOS structures is governed by the trapping/de-trapping mechanisms in the gate dielectric. From the nature and the magnitude of the $1/f$ noise spectra, the physical mechanisms involved as well as the nature of traps and interface qualities can be assessed. From both IETS and $1/f$ noise data the nature of traps and interface properties can be investigated.

In this paper, we report on the interfacial properties of ultrathin (~9 nm) amorphous ALD TiO_2/Al_2O_3 bilayer gate dielectric on $In_{0.53}Ga_{0.47}As$ substrates. Lattice vibrations and phonon modes of $In_{0.53}Ga_{0.47}As$ lattice are studied in detail and are described by analytical expressions; identification of the trap-features including trap-assisted conduction and charge-trapping are performed. The trap features are compared for both the vacuum annealed and as-deposited devices. The low frequency noise study is used to extract trap information and a comparison of $1/f$ noise in vacuum annealed and as-deposited devices is made. Although reports on IETS studies are available in the literature for TiO_2–Al_2O_3/ GaAs systems,[14] reports on phonon modes and lattice dynamics of TiO_2–Al_2O_3/InGaAs systems using IETS are not. In the present work, IETS is used as a non-destructive characterization tools to probe phonons of the substrate, gate-dielectrics, traps and microscopic bonding structures to investigate into the lattice dynamics and interface properties of atomic layer deposited Al/TiO_2–Al_2O_3/ $In_{0.53}Ga_{0.47}As$/InP MOS capacitors.

2. EXPERIMENTAL DETAILS

2.1. Fabrication of ALD Al/TiO_2–Al_2O_3/$In_{0.53}Ga_{0.47}As$/InP MOS Capacitor. Metal-oxide-semiconductor (MOS) capacitors were fabricated on p-$In_{0.53}Ga_{0.47}As$/InP substrates. The wafers were degreased using isopropanol, cleaned in HF solution (1%) for 3 min to remove the native oxide and then dipped in NH_4OH solution for 10 mins. A thin layer of Al_2O_3 was deposited on p-$In_{0.53}Ga_{0.47}As$ using trimethyl aluminium (SAFC Hitech, Haverhill, MA, USA; 99.9%) and H_2O as the precursors in a viscous flow-type (0.6 Torr working pressure) atomic layer deposition equipment (f·XALD ALD equipment, Azimuth Technologies Pte Ltd., Singapore) with a N_2 flow rate of 50 sccm at 170°C. After that, TiO_2 films were deposited under similar conditions. Vapors of $TiCl_4$ (Merck & Co., Inc., Whitehouse Station, NJ, USA; 99%) and H_2O precursors were sequentially introduced into the chamber with an exposure time of 0.1 s and purged by 50-sccm N_2 flow for 10 s between the two exposures. For Al_2O_3 deposition with TMA, 30 cycles were used for the deposition. Typical growth rate was 1 Å/cycle. For the ALD of TiO_2 films, using $TiCl_4$+$2H_2O$ > TiO_2+4HCl reaction, 175 cycles of $TiCl_4$ were used for the deposition of 7 nm TiO_2 with a typical growth rate of 0.4 Å/cycle.[15,16] Vacuum annealing (VA) was carried out for some sample at 350°C for 5 mins at process pressure of $\sim 1 \times 10^{-6}$ mTorr. The Al metal, deposited by evaporation, was used as the gate electrode (area: 2.5×10^{-4} cm^2). Finally, a low resistance ohmic back contact was formed by depositing Au on p-$In_{0.53}Ga_{0.47}As$ substrate by DC sputtering.

dx.doi.org/10.1021/am405019d | ACS Appl. Mater. Interfaces 2014, 6, 3263–3274

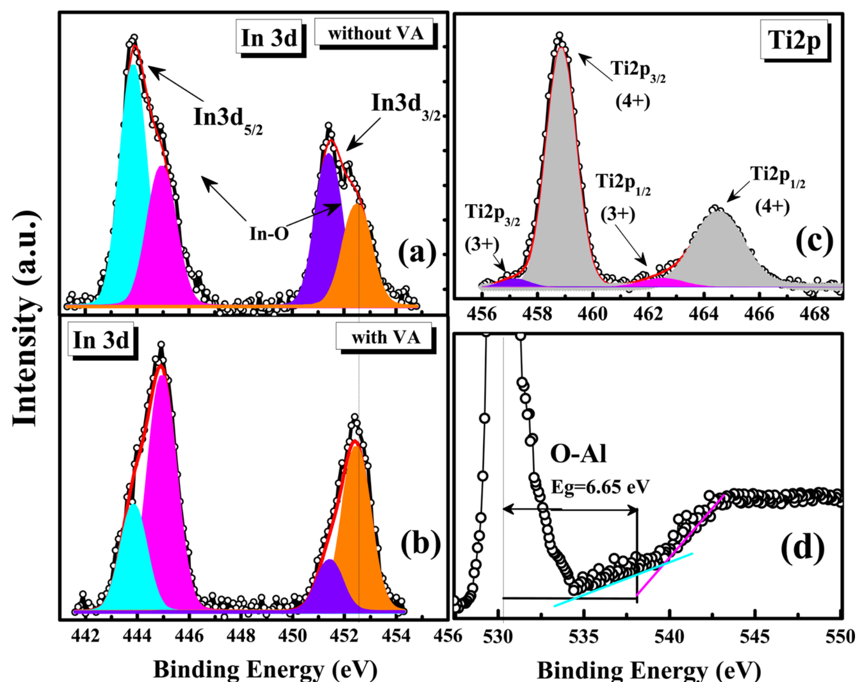

Figure 2. (a, b) In 3d core-level spectra from TiO_2/Al_2O_3 /$In_{0.53}Ga_{0.47}As$ gate stack, with and without vacuum annealing, (c) Ti 2p core-level spectra from $TiO_2/Al_2O_3/In_{0.53}Ga_{0.47}As$, and (d) O 1s energy loss spectra for the TiO_2/Al_2O_3 /$In_{0.53}Ga_{0.47}As$ samples.

2.2. IETS Characterization Setup. The IETS measurements were performed at liquid nitrogen temperature (77K). The setup included an E5263A 2-channel high speed source monitor unit, a SR830 lock-in amplifier and a computer interface to control the bias sources to through GPIB connection and to capture the measured spectra. E5263A 2-channel high speed source monitor unit provided the necessary gate biases through the lock-in amplifier. The spectra were obtained by measuring the second derivatives of the gate tunneling current (I_g) through the metal-insulator-semiconductor tunneling junctions by the SR830 lock-in amplifier detection, with an AC modulation signal (generated from oscillator output of the lock-in amplifier at f = 890 Hz with an amplitude (V_ω) of 2 mV) superimposed on a slowly varying dc gate voltage. The current, thus obtained, is amplified by an operational amplifier. A time constant of 3 s was used in the experiment. A notch filter in the lock-in amplifier was used to remove the unwanted harmonic frequencies.

3. CHARACTERIZATION AND ANALYSES

3.1. Characterization Using XPS. To understand the interface quality between TiO_2/Al_2O_3 and p-$In_{0.53}Ga_{0.47}As$, thin films of TiO_2/Al_2O_3 on p-InGaAs was prepared using the same process recipe and analyzed by x-ray photoelectron spectroscopy high-resolution x-ray photoelectron spectroscopy (XPS) performed under a UHV condition at room temperature with VG ESCALAB 220i-XL XPS system. The take-off-angle was 90° using monochromatic AlK_α (1486.7 eV) excitation sources. Figure 1a−d shows the core-level spectra of Ga 3d and As 3d of TiO_2/Al_2O_3/p-$In_{0.53}Ga_{0.47}As$ for with and without vacuum-annealed sample.

In Figure 1, the indium and gallium bulk peaks are located at ~17.05 and 19.10 eV such that the binding energy separation between the two is fixed at 2.05 eV. There are two peaks attributed to indium oxide, consistent with those seen in the XPS spectra; at 0.57 and 1.15 eV from the bulk peak, again tentatively assigned as In_2O and a mixed phase, $In_xGa_yO_z$ (with $x > y$ initially) respectively.[17] The remaining peaks are due to gallium oxides with a chemical shift at +0.55 eV and +0.85 eV from the bulk Ga peak, attributed to Ga^{1+} (Ga_2O) and Ga^{2+} (GaO).[18] From the Ga 3d spectrum it is evident that Ga−O feature has multiple oxidation states for different samples including Ga^{1+} and Ga^{2+}, probably because of Ga_2O and GaO formation.[19] It is important to note that without annealed sample has resulted in a Ga−O peak that is centered at a lower binding energy for bulk GaAs samples. But for the vacuum-annealed sample the resulting Ga−O feature with low intensity presents in the higher energy position. According to Hinkle et al.,[20] it is possibly due to charge redistribution from second nearest neighbor changes in the Ga−O bonding environment. Thus vacuum annealing can suppress the formation of Ga_2O_x native oxide at the interface with higher oxidation state of Ga, which is more closely related to the interface defects formation, causes to improve the interface quality.[21] The O 2s spectrum consists of the following two peaks: Ga−O−Ti and Ga−O−Al bonds at 22.33 eV, and 23.9 eV attributed to formation of mix bonding in the interface.[22] As the electron affinity of Al is quit higher that of Ti so we have assumed that higher O 2s peak is related with Al−O−Ga. The O 2s spectra of these samples are evident along with Ga3d spectra which are close to reported results.[23]

Arsenic oxide is the well-known species that causes oxide-induced Fermi level pinning through dissociation into As atoms on the GaAs surface.[24] Panels c and d in Figure 1 illustrate the As 3d XPS spectra with fitted Gaussian curves of both the devices with and without vacuum annealing. To obtain a valid fit for the As 3d spectra, we have considered doublets at ~40.03 and ~40.75 eV for metallic As bonding, where they have a peak with a separation of 0.7 eV and As−O with a chemical shift of +9 eV for without vacuum annealed sample indicates that the sample is selectively oxidized during deposition. A model has been proposed by Robertson which describes the defect density of the GaAs and InGaAs surface in terms of Ga and As dangling bonds at the conduction and valence band edges[25] which would support the assignment of these peaks. After vacuum annealing at 350°C all native oxides were completely removed, as shown in Figure 1(d). This result suggests that VA is effective to eliminate

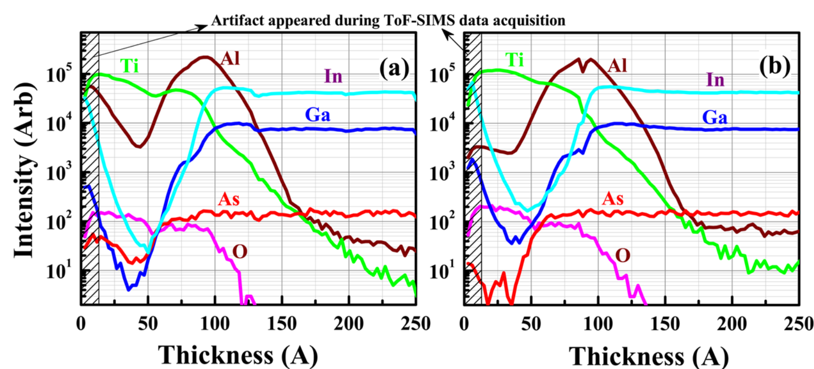

Figure 3. ToF-SIMS profiles of TiO_2/Al_2O_3/InGaAs gate stack for (a) without vacuum annealed, and (b) with vacuum annealed sample.

native oxide and could contribute to improvement of InGaAs MOS interface properties. Additionally strong Ti 3p signal at 36.4−38.2 eV in the As3d region for TiO_2/Al_2O_3 is a further evidence of TiO_2 layer on Al_2O_3 which act as a barrier to As diffusion into the dielectric.[26] Furthermore, after vacuum annealing, the intensity of Ti 3p peaks increases, with a significant shift in the higher binding energy by ∼0.7 eV being concurrently observed. This phenomenon may be correlated with the phenomenon in which the thickness of the barrier layer (BL) region increases because of vacuum annealing, causing significant suppression of arsenic oxides and leading to improvement of InGaAs MOS interface properties. From panels a and b in Figure 1, it can be seen that the ratio of In−As:In_2O_x has been increased, which is due to In related oxide increased after vacuum annealing. In terms of Gibbs free energy of oxide formation, As oxide is less stable than the other oxides such as Ga_2O_3, $GaAsO_4$, In_2O_3, and $InAsO_4$ (As_2O_3, −137.7 kcal/mol; Ga_2O_3, −238.6 kcal/mol; $GaAsO_4$, approximately −223 kcal/mol; In_2O_3, −198.6 kcal/mol; $InAsO_4$, −209.4 kcal/mol).[27] On the basis of our XPS results, after ALD deposition the formation of the undesirable native oxide, especially for arsenic oxide, appears to be significantly suppressed on $In_{0.53}Ga_{0.47}As$ surface.

Panels a and b in Figure 2 show the In 3d spectra for ALD TiO_2/Al_2O_3 gate stack on p-$In_{0.47}Ga_{0.53}As$. In−O bonds were evidenced by fitting G-L curves of the In3d spectra for the sample with and without VA. Oxidation of In after ALD is proved by the In 3d5/2 line decomposition in a bulk peak at 444.45 eV and an In_2O_3 (In^{3+} at 445.56) eV component. However, regardless of the exact assignment of oxidation states, the spectra suggest that the formation of In−O is clearly increased after vacuum annealing sample at 350°C.

Figure 2c illustrates the Ti 2p photoelectron spectra at the surface of the TiO_2 films. Ti 2p XPS spectra before sputtering displays mainly two peaks around 458.7 and 464.5 eV, respectively, assigned to $Ti^{4+}2p_{3/2}$ and $Ti^{4+}2p_{1/2}$ in the TiO_2. The two peaks are located with energy separation of 5.8 eV and from G-L fitting an area ratio of $Ti^{4+}2p_{3/2}$:$Ti^{4+}2p_{1/2}$ was found as 3:1. These results show that the film at the surface is fully oxidized stoichiometric of Ti−O.[28] The shape of the doublet provides a little evidence for presence of non-stoichiometric oxide of $Ti^{3+}2p_{3/2}$ and $Ti^{3+}2p_{1/2}$, which may come from aluminum oxide layer. The extra peaks after 1 min etching indicate the lower contents of O in $Ti^{3+}2p_{3/2}$ and $Ti^{3+}2p_{1/2}$ states in the Ti_2O_3 structure, at around 457.1 and 462.4 eV with the binding energies neighboring to Ti^{4+} states.

The energy band gap of gate dielectrics can be determined from the threshold energy for O1s photoelectron energy loss caused by the interband transition across the energy band gap of the high-*k* dielectrics.[29] As discussed earlier, the broad peak at a higher binding energy of the zero-loss peak can be interpreted within the framework of inter band transition losses, and this can be used to determine the band gap of high-*k* dielectrics. The band gap of the Al_2O_3 and TiO_2 films were determined by the O1s core level spectrum, as shown in Figure 2d. By taking the baseline of energy loss just after the zero-loss peak, the linear extrapolation of the initial slope onset represents the band gap of the oxide. The measured band gaps are expected to be within an error limit of ∼0.05 eV. The band gaps were determined to be 6.65±0.5 eV for Al_2O_3, which are in good agreement with reported values for amorphous phase Al_2O_3.[30]

3.2. ToF SIMS Depth Chemical Analysis. It is important to analyze interdiffusion around the interface for characterization of high-*k* gate dielectric film. The ToF-SIMS technique is highly surface sensitive and gives information from the upper layers to the in depth interface structures of the gate stacks.

Figure 3 shows SIMS depth profile of the As, Ga, and In diffusion in TiO_2/Al_2O_3 gate stacks for the sample with and without vacuum annealing, analyzed with Ar^+ ion beam. From the Figure 3, it can be noticed that As diffusion significantly reduced by one order after vacuum annealing at temperature of 350 °C. This results confirms the As 3d results in previous section. From the XPS analysis it was found that the native oxide consist of Ga_2O_3, In_2O_3, As_2O_3, and elemental As (As−As bonds). After vacuum annealing at 350 °C, the As oxides partially disappear and In_2O_3 are dramatically increased to a level near the detection limit as well as the Ga_2O_3 feature intensity also significantly increases. The reaction paths for Ga oxide decomposition upon the exposure of atomic hydrogen from GaAs native oxide have been discussed by Yamada et al.[31] Partial oxide removal at lower temperatures via the conversion of the stable Ga_2O_3 oxide to a volatile Ga_2O oxide can be roughly explained with the following reaction path:

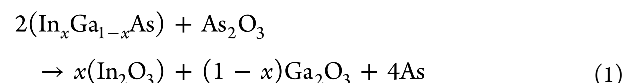

$$2(In_xGa_{1-x}As) + As_2O_3 \rightarrow x(In_2O_3) + (1-x)Ga_2O_3 + 4As \quad (1)$$

$$Ga_2O_3 + 4Ga \rightarrow 3Ga_2O \quad (2)$$

Also from the XPS analysis it can be found that Ga substrate peak intensity increases, whereas the Ga−O bond was reduced. From this finding it seems that Ga_2O_3 partially transform to its lower oxidation state Ga_2O which is also seen from SIMS study. Oxygen transfer from As to Ga and In which has been further confirmed from Figures 1 and 2. Increase in In oxide related species can be seen from panels a and b in Figure 3. Because of artifacts, it seems that In and Al signal concentration slowly

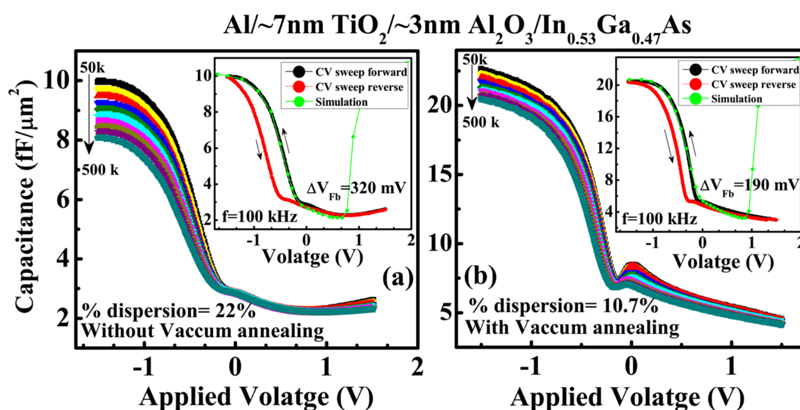

Figure 4. Multi-frequency (50 kHz-500 kHz) $C-V$ characteristics of Al/~7 nm TiO_2/~2 nm Al_2O_3/n-$In_{0.53}Ga_{0.47}As$ MOS capacitors (a) without vacuum annealing (VA) and (b) with VA.

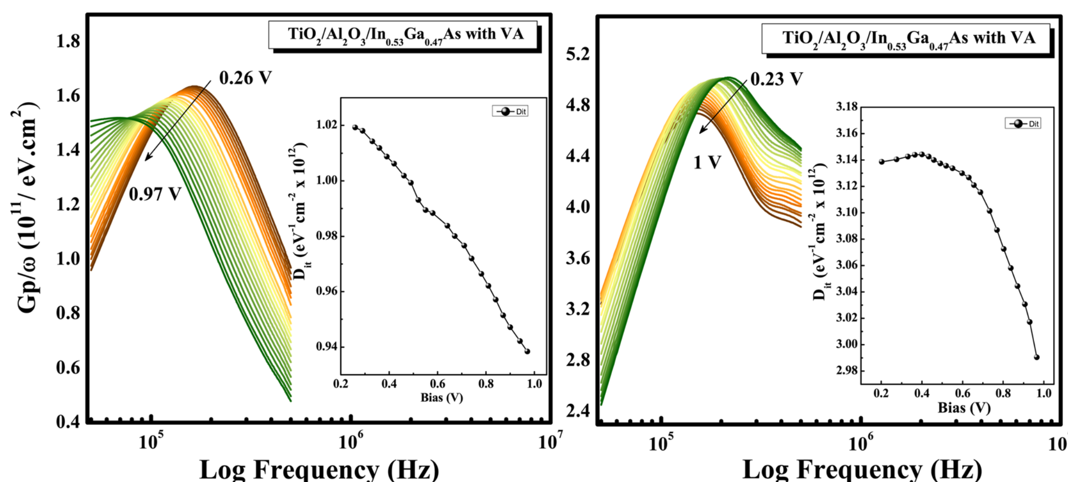

Figure 5. G_p/ω vs log (f) characteristics of Al/TiAlO/GaAs MOS capacitors (a) with and (b) without vacuum annealed sample.

builds up in the interface layer and peaks close to the surface. The first 2 nm close to the surface has been discounted in order to get the meaningful Al and In profiles in gate stack. Though after VA the artifacts becomes less prominent due to the lower concentration oxygen content in the interfacial layer as well as a obstacle to oxygen absorption as indicated by the XPS and SIMS analysis.[32] This result relates our previous XPS experiments (In3d) where the ratio of In−O: In has been significantly increased after vacuum annealing. From eqs 1 and 2, the transformation of As_2O_3 to In_2O_3 and Ga_2O has been shown. This suggests that is it only arsenic oxide that is being removed with vacuum annealing as increased oxygen bond transfer to gallium. So from the SIMS analysis it can be concluded that elementary As can be reduced to improve the electrical property of the gate stack.

3.3. Electrical Characterization. Panels a and b in Figure 4 show the frequency dependent room temperature $C-V$ characteristics of Al/TiO_2/Al_2O_3/p- $In_{0.53}Ga_{0.47}As$ MOS capacitors with and without vacuum annealing. Compared to the MOS capacitors without VA, the $In_{0.53}Ga_{0.47}As$ capacitors with additional VA, exhibit substantially reduced frequency dispersion in accumulation, reduced C−V stretch-out, decreased capacitance response in depletion, and reduced intrinsic carrier response in inversion, indicating that a thin layer of Al_2O_3 can effectively passivate electrically-active defects in Al/TiO_2/Al_2O_3/$In_{0.53}Ga_{0.47}As$ gate stacks. It is also evident that the MOS capacitors with additional VA treatment show a higher maximum accumulation capacitance (C_{ox}) compared to devices without VA. Both the devices show the frequency dispersions in accumulation and depletion regions, as shown in Figure 4.

The amounts of frequency dispersions in accumulation capacitance, evaluated as (C_{ox}), are 22 and 10.7% for with and without VA, respectively. The frequency dispersion in accumulation is attributed to the formation of an inhomogeneous layer at interface between gate dielectric and substrate.[33] From Figure 4, it is noted that the vacuum annealing improved the frequency dispersion by reduced interfacial layer formation. The amounts of frequency dispersion in the depletion region, evaluated as the change of voltage (ΔV) at flatband between 500 and 50 kHz, are 290 and 160 mV for with and without VA devices, respectively. As the frequency dispersion in the depletion region is mainly due to the presence of interface traps, the result indicates that the vacuum annealing reduces the interface trap density.

The hysteresis voltage was determined by sweeping the gate voltage from inversion to accumulation and then sweeping back to obtain the difference of the flatband voltage. This phenomenon is believed to be due to the presence of interfacial electrons and/or mobile charge in the oxide. The hysteresis voltage was found reduce to ~150 mV after VA for TiO_2/Al_2O_3/p-$In_{0.53}Ga_{0.47}$Asstacks, whereas that for as deposited samples was ~330 mV, as shown in Figure 4 (inset).The $C-V$ characteristics for VA devices show a sharper transition from the depletion region to the accumulation region than that obtained in without

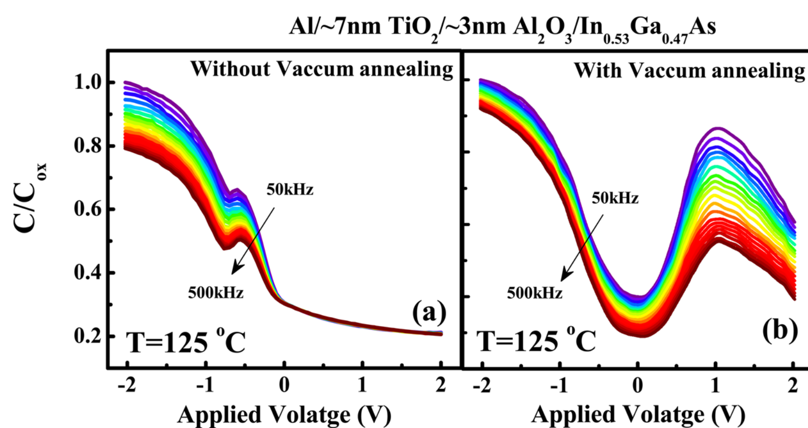

Figure 6. $C-V$ characteristics of Al/∼7 nm TiO_2/∼2 nm Al_2O_3/n-$In_{0.53}Ga_{0.47}As$ MOS capacitors (a) without VA and (b) with VA devices measured at 125 °C.

VA sample, with an excellent $C-V$ curve fitting agreement with a simulated $C-V$ as shown (see Figure 4 inset). The equivalent oxide thickness (EOT) was extracted by fitting the $C-V$ curves in Figure 4 (inset) with the simulated $C-V$ curve that accounts for quantum mechanical effects. The values of EOT are 3.1 and 2.2 nm for with and without VA sample, respectively. The energy distribution of D_{it} was evaluated for MOS interfaces with and without VA by the low-temperature conductance method which utilizes both measured capacitance and extracted parallel conductance data.[34,35]

A conductance method is considered to be the most sensitive method for determining interface trap density (D_{it}). The peak conductance versus frequency $[G_p/\omega - \log(f)]$ curves are shown in Figure 5 in the gate voltage regime from +0.26 to +1 V at frequency range of 50-500kHz. By measuring peak values of equivalent parallel conductance versus frequency required by the high -frequency conductance method, the dependence of D_{it} as a function of the applied voltage is shown in the Figure 4 inset. The D_{it} near the midgap calculated to be about 2.9×10^{12} cm^{-2} eV^{-1} for ALD TiO_2/Al_2O_3/p-$In_{0.53}Ga_{0.47}As$ devices without. The D_{it} of the ALD TiO_2/Al_2O_3/p-$In_{0.53}Ga_{0.47}As$ interfaces decreases by vacuum annealing. The MOS interfaces with VA exhibit D_{it} of the order of $\sim 9 \times 10^{11}$ cm^{-2} eV^{-1} near the midgap. From the distribution of D_{it} around the midgap, for vacuum annealed sample, all D_{it} values lie in the low 1×10^{11} cm^{-2} eV^{-1}, implying good interface quality achieved after vacuum annealing.

It is very difficult for higher band gap materials to extract the extremely slow traps near the midgap that have very low characteristic trapping frequencies for both electrons and holes. As a consequence, these states cannot be probed within the usual frequency range of 100 Hz to 1 MHz An alternative method to evaluate the density of midgap states in GaAs is to thermally activate them at elevated temperature. Hot semiconductor will strongly increase the characteristic emission frequencies. In elevated temperature, it has been shown the possibility to access interface defects over an increased portion of the semiconductor energy gap and assesses their effect on the $C-V$ characteristics.[36]

Figure 6 shows the high temperature (125°C) $C-V$ characteristics of Al/TiO_2/Al_2O_3/p-$In_{0.53}Ga_{0.47}As$MOS capacitors for both with and without VA devices. The accumulation capacitance did not change and the CV curves did not shift horizontally with temperature. The humplike features in Figure 6a may have resulted from the weak inversion due to the increased intrinsic minority carrier generation (n_i) from elevated temperatures (125 °C). The trap response time affect the increased n_i, making the G_p/ω peak of the $G-V$ curves shift towards higher frequencies. In addition, border traps have responses at low measurement frequencies,[37] which correspond to the trap levels near midgap. Thus, the increased contributions to measured G_p/ω may lead to an overestimated D_{it} values obtained at elevated temperatures.

Figure 7 shows the current density-voltage (J-V) characteristics of the InGaAs MOS capacitors measured at V_{FB}-1 V. The

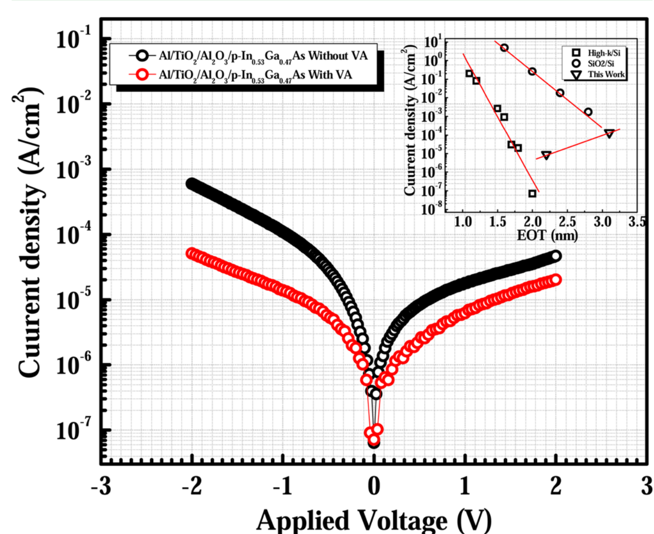

Figure 7. Gate leakage current density vs. gate voltage characteristics of Al/∼7 nm TiO_2/∼2 nm Al_2O_3/n-$In_{0.53}Ga_{0.47}As$ MOS capacitors with and without vacuum annealing.

leakage current density for TiO_2/Al_2O_3/p-$In_{0.53}Ga_{0.47}As$ film is 1×10^{-5}A cm^{-2}, whereas with an EOT of 2.4 nm, vacuum-annealed MOS capacitors demonstrate a low J_G of 1.4×10^{-4}A cm^{-2} at $V_{FB} - 1$ V. The VA TiO_2/Al_2O_3/p-$In_{0.53}Ga_{0.47}As$ gate stacks show a comparable J_G as in recent reports.[38,39] The large decrease, two orders of magnitude in leakage current after VA, is due to suppressed surface states assisted tunneling. Figure 7 inset shows the gate leakage current density at $V_{FB} \pm 1$ V against EOT. The result shows that, even though ALD high-κ on p-$In_{0.53}Ga_{0.47}As$ is leakier than high-κ on Si, it can achieve a comparable or lower leakage current than SiO_2 on Si. With an EOT of 2.3 nm, the p-$In_{0.53}Ga_{0.47}As$ MOS capacitor with vacuum annealing demonstrates a low J_G of $\sim 1 \times 10^{-5}$ A/cm^2 at $V_G = V_{FB} - 1$ V.

4. IETS STUDY OF LATTICE DYNAMICS, TRAPS AND DEFECTS

In this section, we investigate the electron-phonon interaction via inelastic electron tunneling spectroscopy (IETS) measurements in $In_{1-x}Ga_xAs$ samples. The optical-phonon behavior in $In_{1-x}Ga_xAs$ was originally referred to as the "mixed mode" or "one-two mode" by Brodsky and Luckovsky.[40] "InAs-like" features were hardly detected in the spectra at low In contents, and their intensities were found still to be low at higher In contents. $In_{0.53}Ga_{0.47}As$ has two longitudinal optic (LO) and two transverse optic (TO) branches, and both the LO branches exhibit electron-phonon coupling. It is found that the dominant electron-phonon coupling is to the higher-energy 'GaAs-like' LO modes. Due to the original lattice mismatch ($\Delta r/r \approx 7\%$) between GaAs and InAs, structural disorder is superimposed to the chemical disorder in the alloy. $In_{0.53}Ga_{0.47}As$ is near lattice matched to InP substrate; although the substrate-induced strain can cause shift in optical phonon frequencies. There have been several efforts to understand lattice properties of these materials that depend on the effects of biaxial strain and confinement. Disorder-activated TO (DATO) features and effects of microscopic strains on phonon frequency shifts are also needed to be considered.

4.1. Effect of Substrate Strain on Phonon Frequencies and Lattice Dynamics.

The empirical valence force field (VFF) approach[41] offers an attractive alternative over the more accurate ab initio models[42] due to its reduced computational cost for the analysis of physical systems. The simplest and most widely used version of the VFF model was developed by Keating[43] which gives a good description of LO, TO, and LA phonons modes in unstrained covalent semiconductors. For modeling of the electronic states in strained nanostructures,[44] a modified Keating model including anharmonic corrections[45] provides reasonable agreement with the experimental data. The original VFF model for diamond was extended to zinc-blende structures by Martin.[46] Zunger et al. have included the stretch-bend interaction[47,48] and the cross-stretch interaction in successful descriptions of GaP quantum dots,[49] InAs quantum dots,[47] InGaAs alloys and InAs/GaAs super-lattices.[48] Sui et al.[50] described a modified Keating model combined with the six-parameter valence force field (VFF)[51,52] model which describes phonon dispersions in unstrained Si and Ge reasonably well. Steiger et al.[53] unified the VFF descriptions for zinc blend crystals by including all nearest-neighbor as well as the coplanar second-nearest-neighbor interactions, incorporating the Coulomb interaction within the rigid-ion approximation.

In the present work, the modified Keating/VFF model described by Sui et al.[50] is extended for zinc blend structures to describe phonon frequency shifts of "InAs" and "GaAs-like" modes due to strain in $In_{0.53}Ga_{0.47}As$/InP MOS structures and the substrate strain is calculated. Additionally effects of microscopic strain are included and mixed mode behavior of $In_{1-x}Ga_xAs$ is studied. The phonons of the TiO_2/Al_2O_3 dielectrics are also observed from IETS. Optical phonon modes are studied in both in vacuum-annealed and without vacuum anneal devices. A comparative study of the trap-features is presented from IETS results of the two devices. Also $1/f$ noise spectra are compared in the next section to assess the interface qualities of the two devices.

The inelastic peaks are identified from the second derivative $I-V$ spectra. The spectra obtained is an average of eight scans going up to 300 meV after removing the elastic tunneling background. Panels a and b in Figure 8 show the IETS spectra of the two $Al_2O_3/TiO_2/In_{0.53}Ga_{0.47}As$/InP devices depicting the

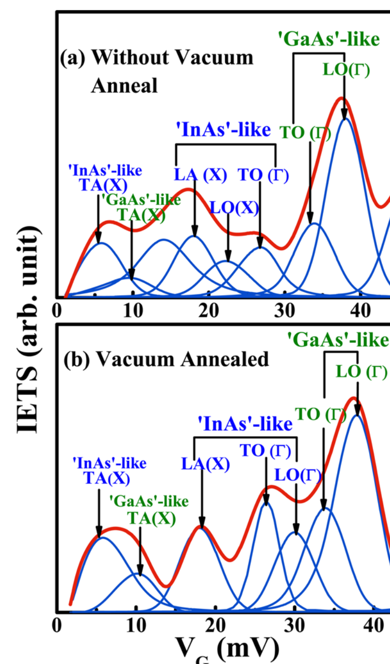

Figure 8. Phonons of "InAs-" and "GaAs-like" modes observed in ALD $Al/TiO_2/Al_2O_3/In_{0.53}Ga_{0.47}As$/InP MOS capacitors from IETS: (a) without vacuum anneal, (b) vacuum-annealed samples.

"InAs" and "GaAs-like" phonon modes. The most intense peak in Figure 8a is found at 37.6 mV (with wave number 303.2 cm^{-1}). This peak is identified as the 'GaAs-like' longitudinal optical phonon (LO) at Γ point. "GaAs-like" transverse optical (TO) phonon at Γ point and transverse acoustic (TA) phonon at X point are observed at 33 mV (wave number 266.1 cm^{-1}) and 9.5 mV (wave number 76.6 cm^{-1}), respectively. The less prominent "InAs-like" phonons are also observed, including the TO (Γ) mode at 27 mV (wave number 217.7 cm^{-1}), the LO (X) mode at 22.5 mV (wave number 181.5 cm^{-}) and TA (X) mode at 6.1 mV (wave number 49.2 cm^{-1}); the longitudinal acoustic (LA) "InAs-like" phonon at X point is found at 17.8 mV (with wave number 143.55 cm^{-1}). Figure 8 (b) also demonstrates the same peaks at almost same voltage locations. All these phonon frequencies demonstrate shift from the phonon frequencies of GaAs and InAs crystals. The strain due to small lattice mismatch as well as internal microscopic strain and mass disorder[54] are accounted for these shifts in phonon frequencies. As a first approach, the phonon frequencies are calculated using dispersion and mode Gruneisen parameters (γ_i).[50] Table 1 lists the analytic expressions of phonon frequencies at the Γ and X points for different modes (which includes quasi-harmonic force constants α, β, κ, and τ, that depend on strain to account for the anharmonic interactions).[42] The phonon frequencies of different modes in InAs[55] and GaAs[53] are also listed in Table 1. Table 2 lists the values of the mode Gruneisen parameters used in the modified Keating model[50] to fit the phonon data.

Under (001) biaxial strain, the elements of strain tensor in the strained-$In_{0.47}Ga_{0.53}As$ film on InP substrate are given as

dx.doi.org/10.1021/am405019d | ACS Appl. Mater. Interfaces 2014, 6, 3263−3274

Table 1. Expressions of Phonon Frequencies in Terms of Quasi-harmonic Force Constants and the Phonon Frequencies of GaAs and InAs

phonon modes	model[42]	GaAs phonon frequencies (cm^{-1})[53]	InAs phonon frequencies (cm^{-1})[55]
$\omega_{LO,TO}$ (Γ)	$\left(\frac{8(\alpha+\beta+\kappa-\tau)}{M}\right)^{1/2}$	TO: 271.13 LO: 293.15	TO: 221 LO: 241
$\omega_{LO,LA}$ (X)	$\left(\frac{4(\alpha+2\beta+\kappa+\tau)}{M}\right)^{1/2}$	LO: 240.3 LA: 225	LO: 199.2 LA: 145.2
ω_{TO} (X)	$\left(\frac{8(\alpha-\tau)}{M}\right)^{1/2}$	256.5	210
ω_{TA} (X)	$\left(\frac{8\beta}{M}\right)^{1/2}$	81.7	53.23

Table 2. Grüneisen Parameters for GaAs and InAs Computed Including Anharmonicity Corrections

material	γ_{LO} (Γ)	γ_{TO} (Γ)	γ_{LO} (X)	γ_{LA} (X)	γ_{TO} (X)	γ_{TA} (X)
InAs	1.06[a]	1.2[a]	1.7527[b]	1.7569[b]	1.956[b]	0.3182[b]
GaAs[c]	1.23	1.39	1.01	1.22	1.73	-1.62

[a]See ref 57. [b]See ref 45. [c]See ref 53.

$$\left.\begin{aligned} e_{xx} &= e_{yy} = \frac{a_{InP} - a_{In_{0.53}Ga_{0.47}As}}{a_{In_{0.53}Ga_{0.47}As}} \\ e_{zz} &= -\frac{2C_{12}}{C_{11}}e_{xx}, \\ e_{xy} &= e_{xz} = e_{yz} = 0, \end{aligned}\right\} \quad (3)$$

where the lattice constants for InP and $In_{(1-x)}Ga_xAs$ with Ga fraction x are given as a_{InP} = 5.8687 Å and $a_{In_{1-x}Ga_xAs}$ = (6.0583 − 0.405x) Å,[56] respectively. For $In_{0.53}Ga_{0.47}As$ films, we have, $a_{In_{0.53}Ga_{0.47}As}$ = 5.86795 Å, which yields e_{xx} = −0.013% (compressive stress). C_{11} and C_{12} are the second-order elastic constants, respectively. Under biaxial strain (001), the expressions for phonon frequencies of TO and LO phonons are expressed in first-order expansion of strain and in terms of Gruneisen parameters (γ_i) developed from the analytic expressions in[50]

$$\begin{aligned} \omega_{TO}(\Gamma) &= \left\{1 + e_{xx}\frac{n_\alpha\alpha_0 + m_\beta\beta_0 + m_\kappa\kappa_0 - n_\tau\tau_0}{2(\alpha_0 + \beta_0 + \kappa_0 - \tau_0)}\right\}\omega_{TO,0}(\Gamma) \\ &= (1 - 3\gamma_{TO}(\Gamma)e_{xx})\omega_{TO,0}(\Gamma) \\ \omega_{LO}(\Gamma) &= \left\{1 + e_{xx}\frac{n_\alpha\alpha_0 + m_\beta\beta_0 + m_\kappa\kappa_0 - n_\tau\tau_0}{2(\alpha_0 + \beta_0 + \kappa_0 - \tau_0)}\right\}\omega_{LO,0}(\Gamma) \\ &= (1 - 3\gamma_{LO}(\Gamma)e_{xx})\omega_{LO,0}(\Gamma) \end{aligned} \quad (4)$$

where the Gruneisen parameters for unstrained InAs and GaAS are listed in Table 2. $\omega_{TO,0}$ (Γ) and $\omega_{LO,0}$ (Γ) are listed in Table 1 for InAs and GaAs. These frequencies are calculated for both InAs and GaAs and the theoretically calculated values of the "InAs" and "GaAs-like" modes are listed in Table 3. At the X point, the LO and LA modes are calculated from the following expressions developed from the original expressions described in[50]

Table 3. Theoretical and Experimental Values of the Phonon Frequencies of "InAs" and "GaAs-like" Modes

phonon frequencies	calcd phonon frequency of "GaAs-like" mode (mV)	calcd phonon frequency of "InAs-like" mode (mV)	exptl values of phonon frequencies from IETS: "GaAs-like" mode (mV)	exptl values of phonon frequencies from IETS: "InAs-like" mode (mV)
ω_{LO} (Γ)	36.4	27.41	37.5	29.4
ω_{TO} (Γ)	33.64	29.9	34.2	26.8
ω_{LO} (X)	29.8	24.72		23
ω_{LA} (X)	27.92	18.01		18
ω_{TO} (X)	31.82	26.06		
ω_{TA} (X)	10.12	6.6	10.04	6

$$\begin{aligned} \omega_{LO}(X) &= \left\{1 + e_{xx}\frac{n_\alpha\alpha_0 + 2m_\beta\beta_0 + m_\kappa\kappa_0 + n_\tau\tau_0}{2(\alpha_0 + 2\beta_0 + \kappa_0 + \tau_0)}\right\}\omega_{LO,0}(X) \\ &= (1 - 3\gamma_{LO}(X)e_{xx})\omega_{LO,0}(X) \\ \omega_{LA}(X) &= \left\{1 + e_{xx}\frac{n_\alpha\alpha_0 + 2m_\beta\beta_0 + m_\kappa\kappa_0 + n_\tau\tau_0}{2(\alpha_0 + 2\beta_0 + \kappa_0 + \tau_0)}\right\}\omega_{LA,0}(X) \\ &= (1 - 3\gamma_{LA}(X)e_{xx})\omega_{LA,0}(X) \end{aligned} \quad (5)$$

The calculated LO and LA frequencies at X point are also listed in Table 3. Similarly, the expressions for TO and TA at X point are also developed using the modified Keating model, and the following expressions are obtained

$$\left.\begin{aligned} \omega_{TO}(X) &= \left\{1 + e_{xx}\frac{n_\alpha\alpha_0 - n_\tau\tau_0}{2(\alpha_0 - \tau_0)}\right\}\omega_{TO_0}(X) \\ &= (1 - 3\gamma_{TO}(X)e_{xx})\omega_{TO,0}(X) \\ \omega_{TA}(X) &= \left\{1 + e_{xx}\frac{m_\beta}{2}\right\}\omega_{TA_0}(X) \\ &= (1 - 3\gamma_{TA}(X)e_{xx})\omega_{TA,0}(X) \end{aligned}\right\} \quad (6)$$

where ω_{TO_0} (X) and ω_{TA_0} (X) are the TO and TA phonon frequencies, respectively, at the X point for both InAs and GaAs as listed in Table 1. From eq 6, the calculated TO and TA are also listed in Table 3. The most significant phonon frequencies obtained from our IETS measurement in the two devices are also listed in Table 3 and they are compared with the theoretically calculated values, both of which are in good agreement. The following empirical expressions are developed for TO and LO phonon frequencies of $In_{1-x}Ga_xAs$ structures using eq 3 and 4 and are given as a function of fraction x for "InAs" and "GaAs-like" modes:

$$\left.\begin{aligned} \omega_{TO}(\Gamma)|_{InAs} &= 245.3 - 51.5x - 3.54x^2\ (cm^{-1}) \\ \omega_{LO}(\Gamma)|_{InAs} &= 265.1 - 50.6x - 3.37x^2\ (cm^{-1}) \\ \omega_{TO}(\Gamma)|_{GaAs} &= 302.1 - 72.2x - 5.08x^2\ (cm^{-1}) \\ \omega_{LO}(\Gamma)|_{GaAs} &= 319.2 - 68.12x - 4.56x^2\ (cm^{-1}) \end{aligned}\right\} \quad (7)$$

In a binary material such as $(InAs)_{1-x}(GaAs)_x$ the collective vibrations of all the harmonic oscillators are described in terms of phonons. We will describe the optical phonons in the $(InAs)_{1-x}(GaAs)_x$ alloy by a set of effective InAs- and GaAs-like oscillators. TO phonons in $In_{1-x}Ga_xAs$ display a two-mode behavior. The TO frequencies in pure GaAs and InAs differ significantly: 271.13 and 221 cm^{-1}, respectively, which is mainly due to the difference between their reduced masses. Hence, it is expected that the GaAs- and InAs-like characters to be preserved

dx.doi.org/10.1021/am405019d | ACS Appl. Mater. Interfaces 2014, 6, 3263−3274

in the alloy. Indeed, when the optical frequencies of the InAs and GaAs binary compounds differ significantly, the Ga atoms are not expected to participate in InAs-like vibrations, and vice versa. The almost linear dependencies of TO frequencies on x fraction can be explained by two effects: mass disorder and microscopic strains.[54] Mass disorder refers to the fact that when one is concerned with the response of one oscillator, the other is at rest, and vice versa. Mass disorder lowers the phonon frequencies.[54] Compressive Microscopic strain increases the phonon frequencies. In our current scope we will focus on the microscopic strain effects on phonon frequencies. A localized mode of In in GaAs lies always in the optical frequency range of the pure compound InAs, whereas, except for some rare "band modes", it is located outside the $In_{1-x}Ga_xAs$ optical range ("local" or "gap" modes).[58] The effect of the host lattice is summed up by an equal stretching of the four bonds of the $InAs_4$ unit, as would be realized by an hydrostatic pressure. A shift $\Delta\omega_{op}$ between the mean value, $\langle\omega_{op}\rangle$ of the InAs optical frequencies to the particular value ω_{op} of the localized mode of $InAs_4$ in $In_{1-x}Ga_xAs$ is induced by this "hydrostatic pressure". If we define an averaged Grüneisen parameter for the optical modes by $\langle\gamma_{op}\rangle$, this shift will satisfy the following equation.[58]

$$\frac{\Delta\omega_{op}}{\langle\omega_{op}\rangle} = -3\langle\gamma_{op}\rangle\left(\frac{\Delta r}{r}\right),$$
$$\omega_{op} = \langle\omega_{op}\rangle + \Delta\omega_{op} \tag{8}$$

where, $(\Delta r/r)$ is the relative change in the bond lengths and $\langle\gamma_{op}\rangle$ the corresponding Grüneisen parameter. For the determination of $\langle\gamma_{op}\rangle$ in either InAs or GaAs, because the Grüneisen parameters are not known for optical modes belonging to any point of the Brillouin zone, the following approximation can be made[58]

$$\langle\gamma_{op}\rangle = \frac{2}{3}\gamma[\mathrm{TO}(\Gamma)] + \frac{1}{3}\gamma[\mathrm{LO}(\Gamma)],$$
$$\langle\omega_{op}\rangle = \frac{2}{3}\omega_{op}[\mathrm{TO}(\Gamma)] + \frac{1}{3}\omega_{op}[\mathrm{LO}(\Gamma)] \tag{9}$$

Table 4 summarizes the average Grüneisen parameters as well the average optical phonon frequencies (calculated using Tables 1 and 2) for InAs and GaAs oscillators due to microscopic strain. The phonon frequency shifts are calculated using $(\Delta r/r)_{GaAs}$ = +1.6x% and $(\Delta r/r)_{InAs}$ = −1.3(1 − x)% according to ref 59. The calculated optical phonon frequencies as well as the corresponding shifts are also summarized in Table 4 for both "InAs" and "GaAs-like" modes. Equation 7 is modified for incorporating the microscopic strain effects and the empirical expressions are given as a function of x fraction as

Table 4. Microscopic Strain Parameters and Phonon Frequencies in $In_{0.53}Ga_{0.47}As$

phonon modes	$\langle\gamma_{op}\rangle$	expression of $\Delta\omega_{op}$	$\langle\omega_{op}\rangle$ (mV)	$\Delta\omega_{op}$ (mV)	$\omega_{TO}(\Gamma)$ (mV)	$\omega_{LO}(\Gamma)$ (mV)
GaAs-like	1.34	+2.22x	28.23	1.043	34.6	37.4
InAs-like	1.153	−1.27(1 −x)	34.53	−0.673	26.7	29.23

$$\left.\begin{aligned}\omega_{TO}(\Gamma)|_{InAs} &= 235.05 - 41.25x - 3.54x^2\ (\mathrm{cm^{-1}})\\ \omega_{LO}(\Gamma)|_{InAs} &= 254.86 - 40.36x - 3.37x^2\ (\mathrm{cm^{-1}})\\ \omega_{TO}(\Gamma)|_{GaAs} &= 302.1 - 54.3x - 5.08x^2\ (\mathrm{cm^{-1}})\\ \omega_{LO}(\Gamma)|_{GaAs} &= 319.2 - 50.22x - 4.56x^2\ (\mathrm{cm^{-1}})\end{aligned}\right\} \tag{10}$$

The LO and TO mode phonon frequencies calculated in Table 4 for the "InAs-" and "GaAs-like" modes are in excellent agreement with the optical phonon modes observed from the experimental IETS data as shown in Table 3.

In panels a and b in Figure 9, the phonons of TiO_2/Al_2O_3 gate stack are shown from IETS results of the two devices (as-deposited and with vacuum anneal devices). The identified peaks of TiO_2 are consistent in the two devices. These peaks include TO phonon at 46 mV (with wave number 371 cm^{-1}) and two LO phonon peaks at 54 and 98 mV (with wave numbers 435.5 and 791.5 cm^{-1}, respectively). The phonon modes observed for TiO_2 agree well with the reported localized vibration of TiO_2 (110).[60] The Al_2O_3 phonons vary slightly in the two devices. In the vacuum annealed sample, the peaks include LO phonons at 62.3, 86, and 103 mV (with wave numbers 502.4, 693.5, and 826.6 cm^{-1}, respectively). The TO phonons are observed at 73.5 and 79 mV (with wave numbers 592.7 and 637.1 cm^{-1}, respectively). In the other sample, the Al_2O_3 LO phonons are observed at 66, 89, 102.1, and 113.8 mV (with wave numbers 532.3, 717.7, 825, and 917.7 cm^{-1}, respectively). The TO phonons are observed at 70, 81, and 85 mV (with wave numbers 564.5, 653.2, and 685.5 cm^{-1}, respectively). The Al_2O_3 phonon modes also agree well with the surface phonons reported for thin aluminium oxide films.[61] The minor phonon shifts may be caused due to the vacuum annealing of the bi-layer TiO_2/Al_2O_3 gate dielectric which reduces the leakage as well as improves the interface quality. This is also reflected in the reduced peak intensities in the vacuum annealed devices as observed from panels a and b in Figure 9.

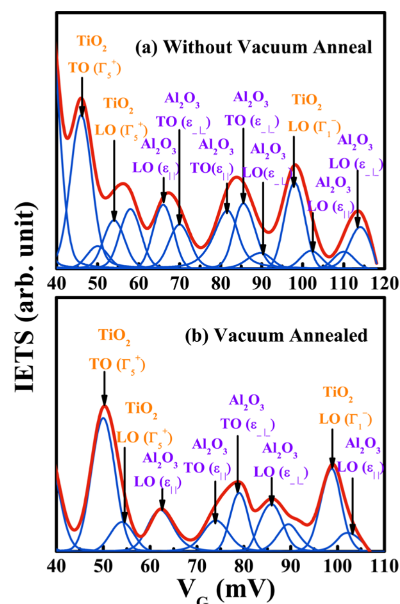

Figure 9. Phonons of TiO_2/Al_2O_3 bi-layer gate stack in ALD Al/TiO_2/Al_2O_3/$In_{0.53}Ga_{0.47}As$/InP MOS capacitors observed from IETS: (a) without vacuum anneal, (b) vacuum annealed samples.

Table 5. Phonons of the TiO_2/Al_2O_3 Gate Dielectric Stack

	phonons	vacuum-annealed sample (cm^{-1})	sample without anneal (cm^{-1})
TiO_2	TO (Γ_5^+)	395.2	371.8
	LO (Γ_5^+)	437.1	435.5
	LO (Γ_1^-)	796	791.5
Al_2O_3	TO ($\varepsilon_\parallel$)	592.7	564.5
	TO ($\varepsilon_\perp$)	637.1	653.2
	TO ($\varepsilon_\perp$)		685.5
	LO ($\varepsilon_\parallel$)	502.4	532.3
	LO ($\varepsilon_\parallel$)	826.6	825
	LO ($\varepsilon_\perp$)	693.5	717.7
	LO ($\varepsilon_\perp$)		917.7

4.2. Trap Study and Evaluation of Interface Quality. Figure 10 shows the IETS spectra of the two $Al/TiO_2/Al_2O_3/In_{0.53}Ga_{0.47}As/InP$ devices (both without anneal and vacuum annealed devices) in the 130−350 mV range. It shows many trap related features. Two distinct trap features are observed; trap-assisted conduction (increased leakage current) and charge trapping (causes shifts in threshold voltage) where the former feature includes a peak followed by a valley and for the later a valley preceding the peak.[13] It is clearly observed that the vacuum annealed sample has less trap features depicting a better quality of the interface compared with the sample without anneal. Also, the leakage is evidently much reduced due to annealing as the peak intensities of the traps in the vacuum-annealed sample are much less. The trap features marked as 1 and 2 in the forward bias are associated with trap-assisted conduction, whereas 3 is associated with charge trapping in the IETS of the vacuum annealed sample. In the sample without anneal, the trap features 1, 2, and 4 are trap-assisted conduction while the feature 3 is charge-trapping. The width of the trap feature is given by $\Delta V = qN_t/C_{ox}$, with N_t being the areal trap density and C_{ox} being the gate dielectric capacitance.[13] Traps that respond in the voltage range 130−350 mV are mainly oxide traps. The major trap features are mainly visible in the 150−200 mV, and in the 250−300 mV ranges. The common interpretation for the origin of these traps is that they may arise due to some characteristics bonding-defects or they may be electrically activated. These can be excited by the energy of the applied voltage and appear in the 2nd derivative of the $I-V$ characteristics as peaks. Proximity of both trap-assisted conduction and charge trapping features (as also observed in Figure 10) may indicate similar origins of the trap states but with slight difference in surroundings.[13]

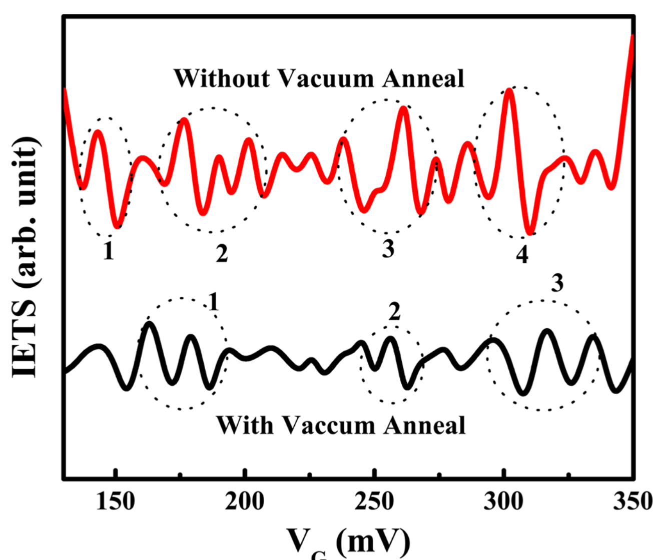

Figure 10. IETS spectra showing trap-features (trap-assisted conduction and charge trapping) in the two ALD $Al/TiO_2/Al_2O_3/In_{0.53}Ga_{0.47}As/InP$ MOS capacitor devices; the trap features and leakage is more prominent in devices without annealing.

5. 1/F NOISE CHARACTERISTICS

The Comparing the trap-features of the vacuum-annealed and without anneal devices from the IETS spectra, it is clear that the leakage and interface quality improves due to vacuum anneal. This is further verified from the $1/f$ noise characteristics of the two devices as depicted in Figure 11. The $1/f$ noise measurement setup includes an Agilent E5263A two-channel high-speed source monitor unit (SMU), a SR 570 LNA, and an Agilent 35670A dynamic signal analyzer. The SMU provides the necessary bias, the minute fluctuations in the current/voltage levels are amplified using the LNA, and the output of the LNA is fed to the dynamic signal analyzer that performs the fast Fourier transform on the time-domain signal to yield the noise power spectral density. The minute fluctuations due to noise were amplified to the measurable range using the low-noise SR570 preamplifier.

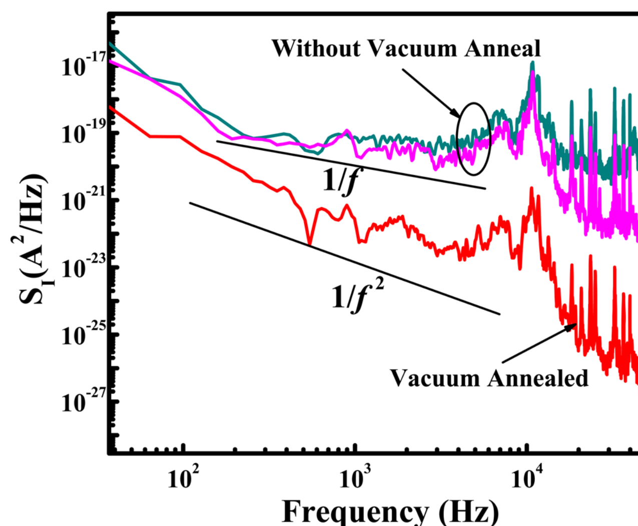

Figure 11. $1/f$ noise current spectra of the ALD $Al/TiO_2/Al_2O_3/In_{0.53}Ga_{0.47}As/InP$ MOS capacitors at a gate bias of −1 V; the vacuum-annealed samples show a lower noise level and a Lorentzian nature of the noise spectral density.

In Figure 11, the current power spectral densities of two different devices, both without anneal, show a significant higher noise level compared to the current spectral density of the vacuum annealed sample. Also, another interesting thing to note is that the devices without anneal, show a $1/f$ dependency on frequency signifying a large number of active traps. While the vacuum annealed sample shows a $1/f^2$ dependency signifying a less number of traps and a better interface quality. A random telegraph noise (RTN) fluctuation is caused due to a single trap and has a Lorentzian ($1/f^2$) power spectral density,[62] when multiple traps are active the superposition of multiple RTNs (Lorentzians) result into a $1/f$ noise spectrum.[63]

dx.doi.org/10.1021/am405019d | ACS Appl. Mater. Interfaces 2014, 6, 3263−3274

6. CONCLUSIONS

In conclusion, TiO_2/Al_2O_3 films on $In_{0.53}Ga_{0.47}As$ substrates by atomic layer deposition and fabrication of $Al/TiO_2/Al_2O_3/In_{0.53}Ga_{0.47}As/InP$ MOS capacitors are reported. The interfacial properties and band alignment have been investigated using XPS. The band gap was determined to be ~6.7 ± 0.05 eV for TiO_2/Al_2O_3. It is shown that the addition of an ultrathin TiO_2 layer on Al_2O_3 helps to reduce of In−O and As−O formation at the interface. Vacuum annealing used for the decomposition and desorption of native oxide (EOT ≈ 2.2 nm) resulted in superior MOSCAP characteristics in terms of low hysteresis and frequency dispersion, moderate D_{it} (~1.5×10^{11} cm^{-2} eV^{-1}) and low leakage current density of 9.1×10^{-6} A cm^{-2} at $V_{FB} - 1$ V.

Inelastic electron tunneling spectroscopy technique was used to study the lattice structure and strain-induced shifts in electron-phonon interactions. Phonon frequencies of the "InAs-" and "GaAs-like" modes are identified from the IETS spectra. Theoretical models for phonon frequencies under strain are validated with experimental IETS data. Empirical relations are developed for phonon frequencies of the TO and LO vibrations of InAs- and GaAs-like modes. Effects of microscopic strain are also incorporated for computation of theoretical TO and LO phonon modes. Trap-features (such as trap-assisted conduction and charge-trapping) and electrically active bonding defects are identified from the IETS in the vacuum annealed (and without) devices. Comparison between the two devices reveals the vacuum annealed devices show a superior interface quality and reduced leakage due to annealing. The phonons of the TiO_2/Al_2O_3 gate stacks are also identified from the IETS. Lastly, the interface qualities are compared with the $1/f$ noise spectra of the two devices which revealed a lower noise level and less active traps in the vacuum annealed devices. Based on the experimental data reported in the present study, ALD high-k TiO_2/Al_2O_3 bilayer may be used as the gate dielectric in future III−V CMOS technology.

■ AUTHOR INFORMATION

Corresponding Authors

*E-mail: tanmoy.das.iitkgp@gmail.com.

*E-mail: dalapatig@imre.a-star.edu.sg.

Present Address

‡C.M. is currently with IMS Laboratory (Laboratoire de l'Intégration du Matériau au Système), University of Bordeaux 1, UMR CNRS 5218. 16, Avenue Pey Berland, 33607 Pessac Cedex, Bordeaux, France

Notes

The authors declare no competing financial interest.

■ REFERENCES

(1) Spicer, W. E.; Chye, P. W.; Skeath, P. R.; Su, C. Y.; Lindau, I. *J. Vac. Sci. Technol.* **1979**, *16*, 1422−1424.

(2) Hasegawa, H.; Akazawa, M. *Appl. Surf. Sci.* **2008**, *255*, 628−632.

(3) Dalapati, G. K.; Chia, C. K.; Mahata, C.; Krishnamoorthy, S.; Tan, C. C.; Tan, H. R.; Maiti, C. K.; Chi, D. *IEEE Trans. Electron Devices* **2013**, *60*, 192−199.

(4) Dalapati, G. K.; Tong, Y.; Loh, W. Y.; Mun, H. K.; Cho, B. J. *IEEE Trans. Electron Devices* **2007**, *54*, 1831−1837.

(5) Frank, M. M.; Wilk, G. D.; Starodub, D.; Gustafsson, T.; Garfunkel, E.; Chabal, Y. J.; Grazul, J.; Muller, D. A. *Appl. Phys. Lett.* **2005**, *86*, 152904−152906.

(6) Chang, C. H.; Chiou, Y. K.; Chang, Y. C.; Lee, K. Y.; Lin, T. D.; Wu, T. B.; Hong, M.; Kwo, J. *Appl. Phys. Lett.* **2006**, *89*, 242911−242913.

(7) Peacock, P. W.; Robertson, J. *J. Appl. Phys.* **2002**, *92*, 4712−4721.

(8) Goel, N.; Majhi, P.; Chui, C. O.; Choi, D.; Harris, J. S. *Appl. Phys. Lett.* **2006**, *89*, 163517−163519.

(9) Dalapati, G. K.; Sridhara, A.; Wong, A. S. W.; Chia, C. K.; Lee, S. J.; Chi, D. Z. *J. Appl. Phys. (Melville, NY, U. S.)* **2008**, *103*, 034508−034512.

(10) Petit, C.; Salace, G. *Rev. Sci. Instrum.* **2003**, *74*, 4462−4467.

(11) Giaever, I.; Megerle, K. *Phys. Rev.* **1961**, *122*, 1101−1111.

(12) Chynoweth, A. G.; Logan, R. A.; Thomas, D. E. *Phys. Rev.* **1962**, *125*, 877−881.

(13) He, W.; Ma, T. −P. *Appl. Phys. Lett.* **2003**, *83*, 5461−5463.

(14) Ma, T. P. *Sci. China, Ser. F* **2011**, *54*, 980−989.

(15) Jevasuwan, W.; Urabe, Y.; Maeda, T.; Miyata, N.; Yasuda, T.; Yamada, H.; Hata, M.; Taoka, N.; M. Takenaka, M.; S. Takagi, S. *Materials* **2012**, *5*, 404−414.

(16) Cameron, M.A.; Gartland, I.P.; Smith, J.A.; Diaz, S.F.; S. M. George, S.M. *Langmuir* **2000**, *16*, 7435−7444.

(17) Sun, Y.; Liu, Z.; Machuca, F.; Pianetta, P.; Spicer, W.E.J. *Vac. Sci. Technol.,A* **2003**, *21*, 219.

(18) Zhu, M.; Tung, C.H.; Yeo, Y. C. *Appl. Phys. Lett.* **2006**, *89*, 202903.

(19) Dalapati, G. K.; Kumar, M. K.; Chia, C. K.; Gao, H.; Wang, B. Z.; Wong, A. S. W.; Kumar, A.; Chiam, S. Y.; Pan, J. S.; Chi, D. Z. J. *J. Electrochem. Soc.* **2010**, *157*, H825−H831.

(20) Hinkle, C. L.; Sonnet, A. M.; Vogel, E. M.; McDonnell, S.; Hughes, G. J.; Milojevic, M.; Lee, B.; Aguirre-Tostado, F. S.; Choi, K.j.; Kim, H. C.; Kim, J.; Wallace, R. M. *Appl. Phys. Lett.* **2008**, *92*, 071901.

(21) Hinkle, C. L.; Milojevic, M.; Brennan, B.; Sonnet, A. M.; Aguirre-Tostado, F. S.; Hughes, G. J.; Vogel, E. M; Wallace, R. M. *Appl. Phys. Lett.* **2009**, *94*, 162101−1162101-3.

(22) Mahata, C.; Mallik, S.; Das, T.; Maiti, C. K.; Dalapati, G. K.; Tan, C. C.; Chia, C. K.; Gao, H.; Kumar, M. K.; Chiam, S. Y.; Tan, H. R.; Seng, H. L.; Chi, D. Z.; Miranda, E. *Appl. Phys. Lett.* **2012**, *100*, 062905−1-062905-4.

(23) O'Connor, E.; Monaghan, S.; Long, R. D.; O'Mahony, A.; Povey, I. M.; Cherkaoui, K.; Pemble, M. E.; Brammertz, G.; Heyns, M.; Newcomb, S. B.; Afanas'ev, V. V.; Hurley, P. K. *Appl. Phys. Lett.* **2009**, *94*, 102902−102904.

(24) Hinkle, C. L.; Sonnet, A. M.; Vogel, E. M.; McDonnell, S.; Hughes, G. J.; Milojevic, M.; Lee, B.; Aguirre-Tostado, F. S.; Choi, K. J.; Kim, H. C.; Kim, J.; Wallace, R. M. *Appl. Phys. Lett.* **2008**, *92*, 071901−071903.

(25) Robertson. *J. Appl. Phys. Lett.* **2009**, *94*, 152104.

(26) Miyazaki, S. *Appl. Surf. Sci.* **2002**, *190*, 66−74.

(27) Hollinger, G.; Skheyta-Kabbani, R.; Gendry, M. *Phys. Rev. B* **1994**, *49*, 11159−11167.

(28) Dhayal, M.; Junb, J.; Guc, H. B.; Park, K. H. *J. Solid State Chem.* **2007**, *180*, 2696−2701.

(29) Miyazaki, S. *J. Vac. Sci. Technol. B* **2001**, *19*, 2212−2216.

(30) Gao, K. Y.; Seyller, Th.; Ley, L.; Ciobanu, F.; Pensl, G.; Tadich, A.; Riley, J. D.; Leckey, R. G. C. *Appl. Phys. Lett.* **2003**, *83*, 1830−1832.

(31) Yamada, M. Jpn. *J. Appl. Phys., Part 2* **1996**, *35*, 651.

(32) Hartmann, J.M.; Benevent, V.; Barnes, J.P.; Veillerot, M.; Deguet, C. *Semiconductor Science and Technology.* **2013**, *28*, 025017.

(33) Harris, H.; Biswas, N.; Temkin, H.; Gangopadhyay, S.; Strathman, M. *J. Appl. Phys.* **2001**, *90*, 5825−5831.

(34) Nicollian, E. H.; Brews, J. R. *MOS (Metal Oxide Semiconductor) Physics and Technology*; Wiley: New York, 2003.

(35) Schroder, D. K. *Semiconductor Material and Device Characterization*; Wiley: New York, 1998.

(36) Brammertz, G.; Martens, K.; Sioncke, S.; Delabie, A.; Caymax, M.; Meuris, M.; Heyns, M. *Appl. Phys. Lett.* **2007**, *91*, 133510−133512.

(37) Fleetwood, D. M.; Winokur, P. S.; Reber, R. A., Jr.; Meisenheimer, T. L.; Schwank, J. R.; Shaneyfelt, M. R.; Riewe, L. C. *J. Appl. Phys.* **1993**, *73*, 5058−5074.

(38) Oh, H. J.; Lin, J. Q.; Lee, S. J.; Dalapati, G. K.; Sridhara, A.; Chi, D. Z.; Chua, S. J.; Lo, G. Q.; Kwong, D. L. *Appl. Phys. Lett.* **2008**, *93*, 062107−062109.

(39) Koveshnikov, S.; Tsai, W.; Ok, I.; Lee, J. C.; Torkanov, V.; Yakimov, M.; Oktyabrsky, S. *Appl. Phys. Lett.* **2006**, *88*, 022106−022108.

(40) Brodsky, M. H.; Luckovsky, G. *Phys. Rev. Lett.* **1968**, *21*, 990−993.

(41) Musgrave, M.; People, J. *Proc. R. Soc. London, Ser. A* **1962**, *268*, 474−484.
(42) Giannozzi, P.; de Gironcoli, S.; Pavone, P.; Baroni, S. *Phys. Rev. B* **1991**, *43*, 7231−7242.
(43) Keating, P. N. *Phys. Rev.* **1966**, *145*, 637−645.
(44) Lee, S.; Lazarenkova, O. L.; Von Allmen, P.; Oyafuso, F.; Klimeck, G. *Phys. Rev. B* **2004**, *70*, 125307−125313.
(45) Lazarenkova, O.; Von Allmen, P.; Oyafuso, F.; Lee, S.; Klimeck, G. *Superlattices Microstruct.* **2003**, *34*, 553−556.
(46) Martin, R. *Phys. Rev. B* **1970**, *1*, 4005−4011.
(47) Williamson, A. J.; Wang, L. W.; Zunger, A. *Phys. Rev. B* **2000**, *62*, 12963−12977.
(48) Kim, K.; Kent, P. R. C.; Zunger, A.; Geller, C. B. *Phys. Rev. B* **2002**, *66*, 045208−045222.
(49) Fu, H.; Ozoliņš, V.; Zunger, A. *Phys. Rev. B* **1999**, *59*, 2881−2887.
(50) Sui, Z.; Herman, I. P. *Phys. Rev. B* **1993**, *48*, 17938−17953.
(51) Tubino, R.; Piseri, L.; Zerbi, G. *J. Chem. Phys.* **1972**, *56*, 1022−1039.
(52) McMurry, H. L.; Solbrig, A. W., Jr.; Boyter, J. K.; Noble, C. *J. Phys. Chem. Solids* **1967**, *28*, 2359−2368.
(53) Steiger, S.; Jelodar, M. S.; Areshkin, D.; Paul, A.; Kubis, T.; Povolotskyi, M.; Park, H. -H.; Klimeck, G. *Phys. Rev. B* **2011**, *84*, 155204−01-155204-11.
(54) Rücker, H.; Methfessel, M. *Phys. Rev. B* **1995**, *52*, 11059−11072.
(55) Talwar, D. N.; Agrawal, B. K. *Phys. Status Solidi B* **1974**, *63*, 441−452.
(56) Adachi, S. *Physical Properties of III−V Semiconductor Compounds*; John Wiley & Sons: New York, 1992.
(57) Groenen, J.; Carles, R.; Landa, G.; Guerret-Piécourt, C.; Fontaine, C.; Gendry, M. *Phys. Rev. B* **1998**, *58*, 10452−10462.
(58) Carles, R.; Landa, G.; Renucci, J. B. *Solid State Commun.* **1985**, *53*, 179−182.
(59) Mikkelsen, J. C.; Boyce, J. B. *Phys. Rev. B* **1983**, *28*, 7130−7140.
(60) Rocker, G.; Schaefer, J. A.; Gopel, W. *Phys. Rev. B* **1984**, *30*, 3704−3708.
(61) Frederick, B. G.; Apai, G.; Rhodin, T. N. *Phys. Rev. B* **1991**, *44*, 1880−1890.
(62) Kirton, M. J.; Uren, M. J. *Adv. Phys.* **1989**, *38*, 367−468.
(63) Haartman, M. V. PhD dissertation, Royal Institute of Technology (KTH), Stockholm, Sweden; 2006.